Mapping genetic interactions in human cancer cells with RNAi and multiparametric phenotyping

Christina Laufer[1,2,4], Bernd Fischer[3,4], Maximilian Billmann[1,2], Wolfgang Huber[3] & Michael Boutros[1,2]

Genetic interactions influence many phenotypes and can be used as a powerful experimental tool to discover functional relationships between genes. Here we describe a robust and scalable method to systematically map genetic interactions in human cancer cells using combinatorial RNAi and high-throughput imaging. Through automated, single-cell phenotyping, we measured genetic interactions across a broad spectrum of phenotypes, including cell count, cell eccentricity and nuclear area. We mapped genetic interactions of epigenetic regulators in colon cancer cells, recovering known protein complexes. Our study also revealed the prospects and challenges of studying genetic interactions in human cells using multiparametric phenotyping.

Often, the combined effect of two genetic variants is not simply the product of the individual effects but rather a buffered or aggravated outcome[1]—generally termed a 'genetic interaction'. Interactions between genes are believed to shape complex phenotypes and can also influence how tumor cells respond to treatment[2,3]. Experimentally, genetic interactions have been systematically uncovered in model organisms: for example, through the use of cell viability as a compound phenotype[4–8]. Focused screens in human cells have been used mainly to detect synthetic lethal interactions for specific mutations[9–12]. We developed a method to systematically analyze genetic interactions of epigenetic regulators in human colon cancer cells using RNAi[13,14] and morphological phenotypes. In total, we performed 51,680 combinatorial RNAi experiments and identified genetic interactions for one or more of 11 phenotypes between 2,376 gene pairs.

RESULTS

Selection of RNAi reagents and multiphenotype assays

We compiled a set of 323 genes implicated in epigenetic regulation, including genes encoding members of chromatin-remodeling complexes or chromatin-modifying enzymes, genes containing domains associated with epigenetic processes, and reported interaction partners of these (**Supplementary Fig. 1** and **Supplementary Table 1**). For each of these genes, we selected three independent siRNAs and quantified their knockdown efficiency by quantitative PCR (qPCR) (**Supplementary Tables 2** and **3**). For 70% of the genes, at least two out of three siRNAs reduced gene expression to <50% (**Supplementary Table 4**). For the combinatorial RNAi experiment, we chose the two siRNAs per gene that had the most similar qPCR values to reduce phenotypic differences due to knockdown efficiency.

We established a workflow for automated analysis of RNAi-induced cell morphology phenotypes at the single-cell level by automated microscopy. For combinatorial RNAi, cells were transfected with all four siRNA combinations per double gene knockdown. After 3 d of RNAi, cells were stained for DNA, α-tubulin and actin (**Fig. 1a**). Multiple quantitative features were computed for each cell. These data included specific cell morphological phenotypes as well as cell number as a measure of overall cell fitness. In total, we extracted 353 phenotypic features per experiment.

A wide range of phenotypes was observed upon knockdown of target genes. For example, depletion of *SETD8*, which encodes a histone 4 lysine 20 (H4K20) methyltransferase also linked to methylation of *PCNA* and to S-phase progression[15,16], led to substantial lengthening of the cells' major axes (**Fig. 1b,c**). In contrast, knockdown of the transcriptional coactivator *TCF20* caused enlargement of the nuclei but not of the cell bodies. In addition, nuclei were rounder than normal, leading to reduced nuclear eccentricity (**Fig. 1d**).

Interaction screen and quality control

To construct genetic interaction profiles, we chose an experimental design to test each of the 323 epigenetic regulators against a subset of genes, which we termed the query genes. Suitable query selection can significantly reduce experiment size while allowing retention of most of the information content[17]. We selected a subset of the target genes such that the phenotypic landscape of their single-gene knockdowns was covered approximately uniformly, as well as according to technical criteria including reproducibility and perturbation efficiency. The selection of these 20 query genes was made on the basis of principal-component analysis of the multivariate phenotypes (**Supplementary Fig. 2**). The combinatorial knockdown screen was performed in two biological replicates. In total, we performed 51,680 pairwise knockdown
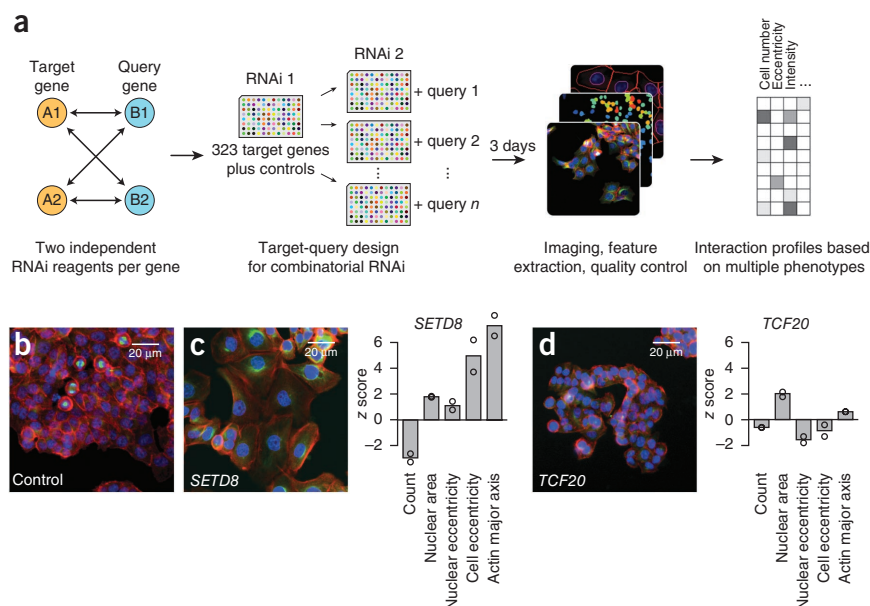
Figure 1 | Combinatorial RNAi and multiparametric phenotyping. (**a**) Screen workflow. (**b**–**d**) HCT116 cells transfected with nontargeting siRNA control (**b**) or with siRNAs targeting *SETD8* (**c**) or *TCF20* (**d**) and stained for DNA (blue), tubulin (green) and actin (red). Bar graphs display five phenotypic features. Circles represent individual replicate measurements.

was measured with a Pearson correlation coefficient of 0.94 between two biological replicates (**Fig. 2a**). Out of the 353 phenotypic features, 227 had a correlation of >0.6 between biological replicates and were considered further (**Fig. 2b**). Because the features were not independent from each other, we identified a subset of nonredundant features by stepwise selection based on linear decomposition (**Supplementary Fig. 3**). In each step of the selection process, the data vector of every available feature was decomposed into two components: the component already spanned by previously selected features and a residual component. The feature with the highest ratio of signal to noise in the residual component was selected, as measured by the correlation between the biological replicates. The process was iterated until no further informative features could be found. This algorithm selected 11 features that contained nonredundant, reproducible phenotypic profiles (**Supplementary Fig. 4**).

experiments by assaying 323×20 target-query gene pairs with 2×2 siRNA designs per gene pair and two biological replicates. Images were acquired at $10\times$ magnification, which allowed for resolution of intracellular structures. Each well was fully covered by four images in each of the three color channels, resulting in 620,160 images. On average, 7,100 cells were imaged and phenotyped per experiment.

Overall, the reproducibility of the phenotypic feature measurements was high: for instance, the eccentricity of the nucleus

In addition, we applied stringent quality control that aimed to address limitations of RNAi such as off-target effects or insufficient on-target knockdown efficiency. We compared the phenotypic profiles, across the set of 20 queries and all phenotypic features, of the two independent siRNAs for each target gene. If off-target effects exist for these siRNAs, they are generally expected to be different, leading to discrepancies between their phenotypic profiles. Moreover, if an siRNA lacks efficiency, its phenotypic profile is dominated by noise. Therefore, we considered
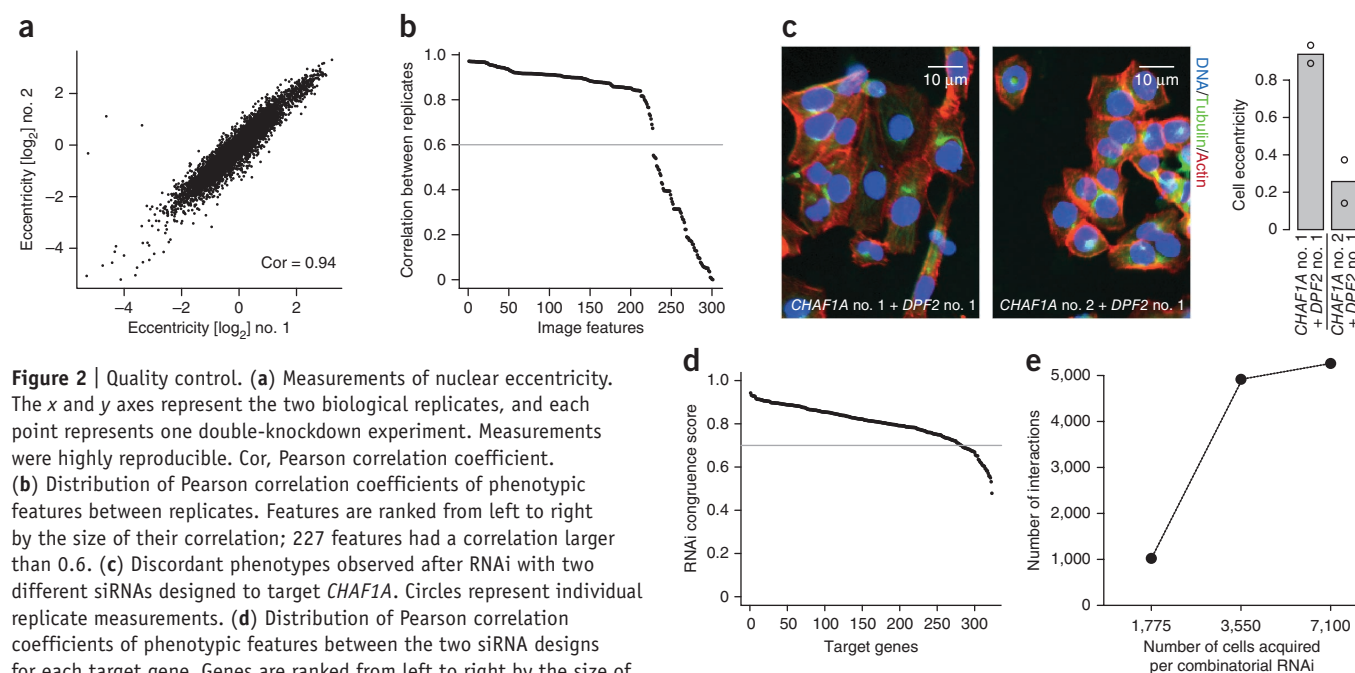
Figure 2 | Quality control. (**a**) Measurements of nuclear eccentricity. The *x* and *y* axes represent the two biological replicates, and each point represents one double-knockdown experiment. Measurements were highly reproducible. Cor, Pearson correlation coefficient. (**b**) Distribution of Pearson correlation coefficients of phenotypic features between replicates. Features are ranked from left to right by the size of their correlation; 227 features had a correlation larger than 0.6. (**c**) Discordant phenotypes observed after RNAi with two different siRNAs designed to target *CHAF1A*. Circles represent individual replicate measurements. (**d**) Distribution of Pearson correlation coefficients of phenotypic features between the two siRNA designs for each target gene. Genes are ranked from left to right by the size of their correlation; 282 genes had a correlation larger than 0.7. (**e**) Simulation of experiments with fewer cells per perturbation condition. The *x* axis represents full- (7,100), half- (3,550) and quarter-size (1,775) data sets. The *y* axis shows the number of interactions detected in each case.

Figure 3 | Genetic interactions. (**a**) Representative image regions for single and double knockdowns of *PHF16* and *SETD8*. Bars display π scores for the feature "actin major axis," a measure of cell-body elongation, for all four siRNA reagent combinations. (**b**) Phenotype-specific genetic interaction of *SIN3A* and *RUVBL1*. Bars display π scores for "nuclear eccentricity." (**c**) Validation of the interaction between *SIN3A* and *RUVBL1* in HeLa cells. Circles in **a**–**c** represent individual replicate measurements; asterisks indicate statistical significance in the moderated *t*-tests (*FDR ≤ 0.05; **FDR ≤ 0.01). (**d**) Overlap of genetic interactions detected from four different phenotypes. Two of the phenotypes shown are derived from cytoskeletal features, and two are nucleus specific.

for each pair of siRNA designs the Pearson correlation coefficient of their phenotypic profiles, computed as the average of per-phenotype correlation coefficients. We termed this measure the siRNA congruence score. A high value of this score suggests that both siRNAs cause a phenotype that is mediated by an on-target effect. The score successfully detected unreliable reagents: for instance, a low score was observed for the two siRNAs targeting *CHAF1A*. Cells treated with one of these two siRNAs (in combination with the same siRNA against *DPF2*) showed different elongation of the cytoskeleton (**Fig. 2c**). Overall, the congruence score was greater than 0.7 for 282 out of 323 genes. These genes were used for further analysis (**Fig. 2d**).

Identification of genetic interactions

To identify genetic interactions, we computed an interaction score, termed the π score[18,19], that measures the difference between the prediction from the non-interacting model and the observed value (Online Methods). For interaction calling, we used a moderated *t*-test on the biological replicates for each siRNA pair and phenotypic feature[20]. This statistical test procedure is adapted to settings with small sample size but large number of similar tests. The tests detected 5,262 genetic interactions at a false discovery rate of 1%; these interactions were between 2,376 gene pairs (**Supplementary Table 5**). The appropriateness of the non-interacting model and of the parameter fitting was assessed by a sparsity criterion: most π scores were small, and for most of the 284,240 tests performed (for all combinations of 323 target genes, 20 query genes, 4 siRNA pairs and 11 phenotypes), no interaction was called, indicating that the bulk of data were fit by the non-interacting model and that interaction calls were specific. Batch effects can complicate the analysis of genetic interaction data sets[7]. We confirmed the absence of strong batch effects with diagnostic plots (**Supplementary Fig. 5**).

The number of cells assayed per double perturbation, which was 7,100 on average, was a critical parameter for the experiment's sensitivity. We investigated the role of this parameter by repeating the analysis with subsampled data sets, using one-half and one-quarter of the cells imaged, corresponding to 3,550 and 1,775 cells per experiment on average. With these reduced data, the number of interactions called decreased substantially, dropping to 1,022 (19%) for the smaller set of cells (**Fig. 2e**). This strong dependence reflects the fact that the scale of the interactions was generally much smaller than the scale of the phenotypes themselves, requiring high precision of the phenotype measurements. This observation may serve as a guideline for the design of combinatorial RNAi experiments.
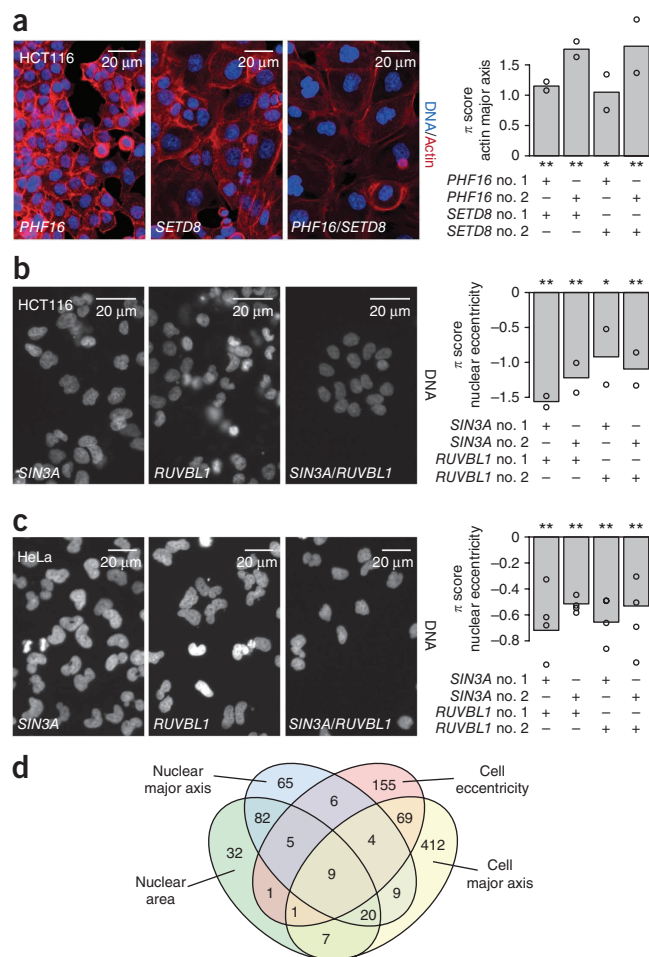
Genetic interactions were specific for phenotypic features

Although for some gene pairs, interactions were detected across multiple phenotypic features, we observed many cases in which phenotype-specific patterns emerged. For instance, knockdown of *SETD8* led to elongation of the cell's major axis; knockdown of *PHF16* had no effect on this feature; and perturbation of both genes led to a significantly larger cell body, indicating a positive genetic interaction (**Fig. 3a**). Similarly, the single perturbations of *SIN3A* and *RUVBL1* yielded normally shaped nuclei, whereas combined depletion led to reduced nuclear eccentricity (**Fig. 3b**). In contrast, neither gene pair showed a significant genetic interaction for cell number. These examples show how acquiring genetic interactions for multiple different phenotypes provides increased sensitivity and specificity.

We retested an exemplary interaction, between *SIN3A* and *RUVBL1*, with independent RNAi reagents and a different cell line. Analysis of nuclear eccentricity after single and double knockdowns of these genes with pools of four independent siRNAs from a different library (Dharmacon) confirmed the negative interaction between the genes that we found in the screen (π score = −0.59, *P* = 0.003, *t*-test). Furthermore, we validated this genetic interaction in HeLa cells using the same RNAi reagents as in the screen. All four combinations of siRNAs targeting *SIN3A* and *RUVBL1* yielded cells with a significantly lower nuclear eccentricity than expected, indicating that *RUVBL1* and *SIN3A* show the same interaction in HeLa cells as in the HCT116 cells used in the screen (**Fig. 3c**).

Figure 4 | Genetic interaction profiles. (**a**) Heat map overview of all measured interactions (π scores). π scores for each feature were scaled to median deviation 1. The rows (*y* axis) correspond to 564 siRNAs targeting the 282 quality-controlled template genes, the columns (*x* axis) to 40 siRNAs targeting 20 query genes, times the 11 non-redundant phenotypic features. (**b**) Density plots (smoothed histograms) of the Pearson correlation coefficients between interaction profiles of siRNAs targeting different genes (red) and between siRNAs targeting the same gene (blue). For the latter, the set of genes was restricted to those with information-rich profiles, defined as containing at least five π scores with $\pi > 5$. High correlation coefficients of the interaction profiles suggest on-target specificity of RNAi reagents. Tick marks show individual correlation values for same-gene pairs. (**c**) Unsupervised cluster analysis of the information-rich gene interaction profiles. Clustering was performed according to the Pearson correlation of gene interaction profiles. Three clusters with functionally related genes identified from positive correlation of interaction profiles are shown.


We found that the screen-wide overlap of genetic interactions between phenotypic features associated with the same cellular compartment was higher than that for features of different compartments, for example, cell major axis and nuclear major axis (**Fig. 3d**).

Genetic interaction profiles and functional analysis

For each target gene siRNA, we obtained a genetic interaction profile comprising the interactions with all query genes with respect to the 11 phenotypes (**Fig. 4a**). Interaction profiles of the two independent siRNA designs per target gene were highly correlated in those cases in which the profiles showed sufficient signal (**Fig. 4b**). Unsupervised clustering of these genes based on the Pearson correlation of their interaction profiles revealed several clusters of well-characterized function (**Fig. 4c**). For example, one cluster contained genes encoding three members of the TIP60 acetyltransferase chromatin remodeling complex, *EP400*, *ACTL6A* and *TRRAP*[21]. In another cluster, we found genes encoding three (out of six) proteins containing an acetylated lysine–binding bromodomain, thereby suggesting a functional connection. A further cluster comprised genes for two common members of the SWR1 and INO80 chromatin remodeling complexes, *RUVBL1* and *RUVBL2* (ref. 22), and the mRNA splicing factors *PHF5A* and *CDC5L*[23,24]. These findings indicate that gene functions can be inferred from genetic interaction profiles generated by siRNAs.

DISCUSSION

Genetic interaction analysis is a powerful approach to functionally connect genes on the basis of their combined contributions to phenotypic outcomes. Our study also outlines challenges and provides guidelines for the design of comprehensive genetic interaction experiments in human cells. First, we calculated an siRNA congruence score based on multiple sequence-independent reagents and their multiparametric phenotypes.
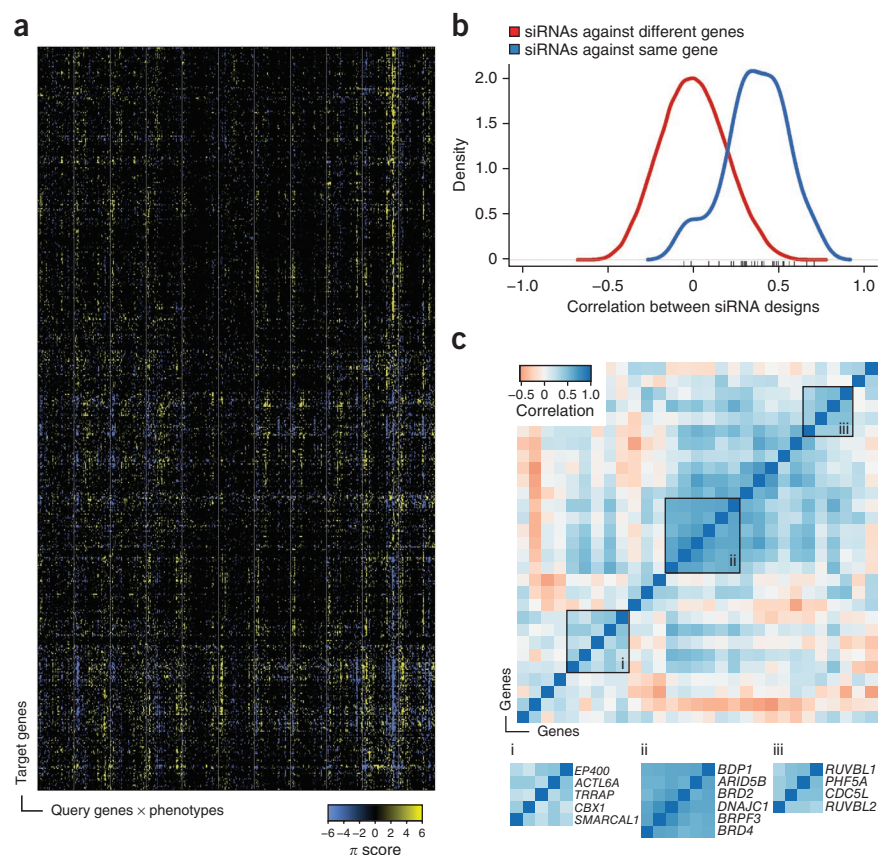
This quality-control step allowed to us to remove perturbations from further analysis that showed inconsistent phenotypes due to off-target effects or knockdown inefficiencies. Second, we ran multiple biological replicates and phenotyped large numbers of individual cells (>5,000) in each experiment. Single-cell phenotyping of a sufficient number of cells is crucial and has a direct impact on the sensitivity of the interaction analysis. Third, we believe that saturation effects are negligible because the fitted interaction matrix is sparse. Although these considerations increase the size of genetic interaction experiments, we have implemented two key experimental design strategies that can ameliorate these limitations. We believe that single-cell, multiparametric phenotyping provides the experimental and computational means to filter against experimental artifacts and is a rich source of genetic interactions. In addition, using asymmetric interaction matrices and a target-query design with a selected set of queries based on divergent phenotypes reduces the size of the interaction matrices. Although pooled short hairpin RNA screens provide an alternative concept for the measurement of genetic interactions and have the advantage of easier scalability[25–27], such approaches are limited to selectable phenotypes, such as cell fitness. In contrast, well-based approaches allow the phenotyping of single cells beyond cell number and can contribute epistatic information on multiple (parallel) processes.

Several differences between genetic interaction experiments in human cells and those in model organisms are noteworthy. On a technical level, we observed that knockdown efficiencies for human cells were lower and off-target effects more widespread than in *Drosophila melanogaster* cells[18], thus requiring additional computational filtering and an additional step in the experimental design,

wherein multiple RNAi reagents are pre-evaluated according to the phenotype-based RNAi congruence score. As compared to genetic interaction experiments in yeast, we found no strong preference for positive or negative interactions with any of the 11 phenotypic features (**Supplementary Fig. 6**). In yeast, genome-scale double knockouts assayed for the colony size phenotype showed a preference for aggravating interactions[4]. The reasons for this difference remain to be understood; possible explanations could include the hypomorphic nature of knockdowns as compared to genetic lesions (as in yeast) and higher genetic redundancy.

Although scaling well-based genetic interaction experiments to a genome-wide analysis in human cells will present significant technical challenges, we believe that focused genetic interaction experiments provide a powerful method to dissect the reorganization of cellular networks, such as that triggered by cancer-associated genetic variants. Image-based phenotyping and asymmetric experimental design allow measurement of the contribution of genes beyond classical synthetic lethality analysis. As different platforms to measure genetic interactions in human cells are becoming available[27,28], large-scale mapping of genetic interactions promises to increase our understanding of biological systems in health and disease.

METHODS
Methods and any associated references are available in the online version of the paper.

Accession codes. The data and the R scripts for analysis are available as R/Bioconductor package HD2013SGI from http://www.bioconductor.org/.

Note: Supplementary information is available in the online version of the paper.

1. Hartman, J.L. IV., Garvik, B. & Hartwell, L. Principles for the buffering of genetic variation. *Science* **291**, 1001–1004 (2001).
2. Farmer, H. *et al.* Targeting the DNA repair defect in *BRCA* mutant cells as a therapeutic strategy. *Nature* **434**, 917–921 (2005).
3. Huang, S. *et al.* MED12 controls the response to multiple cancer drugs through regulation of TGF-β receptor signaling. *Cell* **151**, 937–950 (2012).
4. Costanzo, M. *et al.* The genetic landscape of a cell. *Science* **327**, 425–431 (2010).
5. Dixon, S.J., Costanzo, M., Baryshnikova, A., Andrews, B. & Boone, C. Systematic mapping of genetic interaction networks. *Annu. Rev. Genet.* **43**, 601–625 (2009).
6. Bandyopadhyay, S. *et al.* Rewiring of genetic networks in response to DNA damage. *Science* **330**, 1385–1389 (2010).
7. Baryshnikova, A. *et al.* Quantitative analysis of fitness and genetic interactions in yeast on a genome scale. *Nat. Methods* **7**, 1017–1024 (2010).
8. Nichols, R.J. *et al.* Phenotypic landscape of a bacterial cell. *Cell* **144**, 143–156 (2011).
9. Bernards, R. A missing link in genotype-directed cancer therapy. *Cell* **151**, 465–468 (2012).
10. Brough, R. *et al.* Functional viability profiles of breast cancer. *Cancer Discov.* **1**, 260–273 (2011).
11. Luo, J. *et al.* A genome-wide RNAi screen identifies multiple synthetic lethal interactions with the Ras oncogene. *Cell* **137**, 835–848 (2009).
12. Sandmann, T. & Boutros, M. Screens, maps & networks: from genome sequences to personalized medicine. *Curr. Opin. Genet. Dev.* **22**, 36–44 (2012).
13. Boutros, M. & Ahringer, J. The art and design of genetic screens: RNA interference. *Nat. Rev. Genet.* **9**, 554–566 (2008).
14. Boehm, J.S. & Hahn, W.C. Towards systematic functional characterization of cancer genomes. *Nat. Rev. Genet.* **12**, 487–498 (2011).
15. Houston, S.I. *et al.* Catalytic function of the PR-Set7 histone H4 lysine 20 monomethyltransferase is essential for mitotic entry and genomic stability. *J. Biol. Chem.* **283**, 19478–19488 (2008).
16. Wu, S. *et al.* Dynamic regulation of the PR-Set7 histone methyltransferase is required for normal cell cycle progression. *Genes Dev.* **24**, 2531–2542 (2010).
17. Casey, F.P., Cagney, G., Krogan, N.J. & Shields, D.C. Optimal stepwise experimental design for pairwise functional interaction studies. *Bioinformatics* **24**, 2733–2739 (2008).
18. Horn, T. *et al.* Mapping of signaling networks through synthetic genetic interaction analysis by RNAi. *Nat. Methods* **8**, 341–346 (2011).
19. Mani, R., St Onge, R.P., Hartman, J.L. IV., Giaever, G. & Roth, F.P. Defining genetic interaction. *Proc. Natl. Acad. Sci. USA* **105**, 3461–3466 (2008).
20. Smyth, G.K. Linear models and empirical Bayes methods for assessing differential expression in microarray experiments. *Stat. Appl. Genet. Mol. Biol.* **3**, 3 (2004).
21. Doyon, Y. & Cote, J. The highly conserved and multifunctional NuA4 HAT complex. *Curr. Opin. Genet. Dev.* **14**, 147–154 (2004).
22. Morrison, A.J. & Shen, X. Chromatin remodelling beyond transcription: the INO80 and SWR1 complexes. *Nat. Rev. Mol. Cell Biol.* **10**, 373–384 (2009).
23. Ajuh, P. *et al.* Functional analysis of the human CDC5L complex and identification of its components by mass spectrometry. *EMBO J.* **19**, 6569–6581 (2000).
24. Rzymski, T., Grzmil, P., Meinhardt, A., Wolf, S. & Burfeind, P. PHF5A represents a bridge protein between splicing proteins and ATP-dependent helicases and is differentially expressed during mouse spermatogenesis. *Cytogenet. Genome Res.* **121**, 232–244 (2008).
25. Lin, Y.Y. *et al.* Functional dissection of lysine deacetylases reveals that HDAC1 and p300 regulate AMPK. *Nature* **482**, 251–255 (2012).
26. Marcotte, R. *et al.* Essential gene profiles in breast, pancreatic, and ovarian cancer cells. *Cancer Discov.* **2**, 172–189 (2012).
27. Bassik, M.C. *et al.* A systematic mammalian genetic interaction map reveals pathways underlying ricin susceptibility. *Cell* **152**, 909–922 (2013).
28. Roguev, A. *et al.* Quantitative genetic-interaction mapping in mammalian cells. *Nat. Methods* advance online publication, doi:10.1038/nmeth.2398 (13 February 2013).

ONLINE METHODS

Cell culture conditions. HCT116 cells were obtained from the ATCC and propagated in McCoy's 5a modified medium (Life Technologies) supplemented with 10% FBS (Biochrom) at 37 °C, 5% CO_2. Subcultivation was performed every 2–3 d at a ratio of 1:5 to 1:10. HeLa cells were obtained from ATCC and propagated in Dulbecco's modified Eagle medium (DMEM) (Life Technologies) supplemented with 10% FBS (Biochrom) at 37 °C, 5% CO_2. Subcultivation was performed every 2–3 d at a ratio of 1:10 to 1:20.

Quantification of siRNA knockdown efficiency by qPCR. Cells were reverse transfected with siRNAs in 96-well plates using Dharmafect 1 transfection reagent (Dharmacon) according to the manufacturer's instructions. In brief, we combined 10 µl siRNA (100 nM) with 30 µl of transfection mix (0.1 µl Dharmafect 1 in RPMI 1640 medium) and incubated the mixture for 30 min at room temperature. After complex formation, 10,000 cells in 60 µl McCoy's medium were seeded per well and incubated for 3 d at 37° C. For quantitative PCR (qPCR) analysis, cells were lysed in 20 µl QuickExtract RNA extraction solution (Epicentre). Lysate (11 µl) was used for cDNA synthesis with the Revertaid cDNA synthesis kit (Fermentas) using oligo(dT) primers. qPCR reactions were performed in duplicate with the Universal ProbeLibrary system (Roche Applied Biosciences) according to the manufacturer's instructions and analyzed using the manufacturer's software. Intron-spanning primers were designed with the Universal ProbeLibrary Assay Design Centre (**Supplementary Table 3**). All qPCR experiments were carried out in three biological replicates. Of all siRNAs, 68% caused a reduction in transcript level to <50%. For 47% of genes, three out of three siRNAs, and for 23% of genes, two out of three siRNAs reduced transcript levels to <50%.

Selection of siRNAs. The siRNAs for the combinatorial RNAi were selected from the Ambion siRNA library, which comprises three individual nonoverlapping siRNA designs for each gene (**Supplementary Table 2**). We chose two siRNA designs per gene on the basis of their qPCR results in the single knockdowns. To avoid strong efficiency differences between the siRNA designs, we selected the two siRNAs with most similar mRNA levels upon knockdown. For 36 of 323 genes, incomplete qPCR analysis results were obtained, and we chose either the best-performing design plus one randomly chosen design, siRNAs validated by the manufacturer or two randomly chosen designs (**Supplementary Table 4**).

Combinatorial RNAi. For the double knockdowns we plated 2×2.5 µl of siRNAs (200 nM) in 384-well clear-bottom microscopy plates (BD Biosciences). First, we transferred aliquots of the siRNAs targeting the 323 target genes, distributing the two individual designs onto separate plates. Then we added one of the query siRNAs to each template plate, creating 25,840 RNAi combinations per replicate. The combinatorial RNAi was performed in two biological replicates yielding a total of 51,680 combinatorial knockdowns. HCT116 cells were reverse transfected using Dharmafect 1 transfection reagent (Dharmacon) according to the manufacturer's instructions. Briefly, 5 µl of siRNAs (200 nM) were incubated for 30 min with 15 µl of transfection mix (0.05 µl Dharmafect 1 in RPMI-1640 medium), and then 1,750 cells in 30 µl McCoy's medium were seeded into each well and incubated for 3 d at 37 °C.

Cell staining and imaging. Cell staining was performed using a Biomek FX robot with 384-well tip head. After 3 d cells were fixed and permeabilized with 5% paraformaldehyde (Sigma), 0.2% Triton X-100 (Sigma) for 45 min at room temperature. To prevent nonspecific antibody binding, cells were incubated with 3% bovine serum albumin (Gerbu), 0.05% Triton X-100 for 30 min. Nuclei, tubulin and actin were stained with 2 µg/ml Hoechst 33342 (Invitrogen), anti-tubulin antibody labeled with fluorescein isothiocyanate (Sigma, catalog number F2168, clone DM1A, 1:750) and 67 ng/ml phalloidin labeled with tetramethylrhodamine isothiocyanate (Sigma) in blocking solution at 4 °C overnight. Cells were washed four times with PBS, and 0.05% sodium azide (Sigma) was added for storage. Plates were sealed with aluminum sealing tape (Corning) and stored until imaged at 4 °C while protected from light. Fluorescence images were acquired with an InCell Analyzer 2000 (GE Healthcare) at 10× magnification. To cover each well fully, we imaged four sites per well, resulting in a total of 620,160 images.

Image processing and feature extraction. Images were obtained from the InCell Analyzer 2000 as 12-bit TIFF images of size 2,048 pixels × 2,048 pixels at three colors. The data set comprised 5.6 terabytes. We adapted image segmentation and feature extraction methods from previous work[29–31], using the R package EBImage[32]. Nuclei were segmented by adaptive thresholding with a window size of 10 pixels (corresponding to 7.4 µm) and subsequent morphological filters. Nucleus segmentation was extended to the cell body by a Voronoi tessellation–based propagation algorithm[33]. Features for intensity, shape and texture were extracted for each cell from the DAPI channel using the nucleus segmentation and from the actin and tubulin channels using the mask of the cell body. Additional features were extracted from the joint distribution of the DAPI and the tubulin signals using the cell body mask. Features were summarized per experiment by the arithmetic mean over all cells. The number of segmented nuclei was used as a proxy for cell count. Features were transformed to a generalized logarithm (glog) scale as suggested by Huber *et al.*[34].

Selection of nonredundant features. We first manually selected the count feature. To select further phenotypic features, we used a stepwise feature-selection algorithm. In each step, we performed a linear decomposition of each remaining feature into (i) the component contained in the subspace spanned by the already selected features and (ii) the residuals. To assess the signal-to-noise ratio of the residual components, we computed the Pearson correlation between their biological replicates and chose the feature with the highest correlation. To define a stopping criterion, we noted that if all features were to contain random data, the distribution of correlation coefficients would be symmetric around 0. Therefore, we terminated the feature selection once the number of negatively correlated candidate features exceeded that of positively correlated ones.

Genetic interaction scores and statistical analysis. Single-gene effects (main effects) were computed by robust fit of a linear combination of the two main effects for each glog-transformed

measurement with an L1-loss function. This model corresponds to a multiplicative model on the original feature scale[18,35], in which the expected outcome for a non-interacting gene pair is the product of the two main effects. Following Horn *et al.*[18], we limited the impact of potentially remaining subtle batch effects on our interaction estimates through the target-query experimental design: effects that influenced whole plates were absorbed by the query effect estimates, and effects associated with particular spatial positions in the plates (for example, subtle edge effects) were absorbed by the target effect estimates, leaving interaction estimates unaffected. Main effects were estimated for each siRNA reagent and independently for each phenotypic feature. Model fit was verified by small size, symmetry and lack of correlation of the fit residuals. To filter out experimental artifacts, we discarded measurements whose replicates differed by more than four times the median of the absolute value of all differences between the two replicates. Genetic interaction scores (π scores) were calculated as the difference (on the glog scale) between the observed phenotype and the expected (non-interaction) value. To test scores for statistical significance, we used the two biological replicates and computed *P* values with the moderated *t*-test of the R package limma[20]. This test is adapted for settings with a small sample size but a large number of similar tests, as through the use of an empirical Bayes variance estimator it overcomes the problem of large variability that, for instance, the usual *t*-statistic has in this setting. *P* values were corrected for multiple testing by the method of Benjamini-Hochberg[36], which controls the false discovery rate. A cutoff on the adjusted *P* values of 0.01 is applied to call genetic interactions (columns "padj" in **Supplementary Table 5**).

Validation of the interaction between *SIN3A* and *RUVBL1*.
For validation with Dharmacon siRNA pools, HCT116 cells were reverse transfected as described above in four replicates. For double knockdowns, cells were transfected with 2×2.5 µl of siRNA pools (500 nM each); for single knockdowns, cells were transfected with 2.5 µl of siRNA pool (500 nM) targeting *SIN3A* or *RUVBL1* together with 2.5 µl of control siRNA (500 nM) targeting *Renilla* luciferase (RLuc). Catalog numbers of the used RNAi reagents are

M-012990-00 (*SIN3A*), M-008977-00 (*RUVBL1*) and P-002070-01-20 (RLuc). For the validation in HeLa cells, cells were reverse transfected in four replicates. For double knockdowns, the 2×2 Ambion siRNA designs targeting *RUVBL1* and *SIN3A* were combined in all four possible ways using 2.5 µl (200 nM) of each siRNA. For single knockdowns, 2.5 µl of siRNAs targeting *SIN3A* or *RUVBL1* were combined with 2.5 µl of nontargeting siRNA control (200 nM). Reverse transfection was performed as described above with the exception of using Lipofectamine RNAiMAX (Life Technologies) instead of Dharmafect 1 transfection reagent under otherwise unchanged conditions. After complex formation, 1,250 cells in 30 µl DMEM were seeded into each well and incubated for 3 d at 37 °C. Cell staining, imaging, image analysis and feature extraction were performed as described above. Baseline and main effects were computed from nontargeting controls and single-gene knockdowns for each siRNA design. π scores were computed using a log-additive model as above. *P* values were computed by a *t*-test over four replicates for HeLa cells.

29. Carpenter, A.E. *et al.* CellProfiler: image analysis software for identifying and quantifying cell phenotypes. *Genome Biol.* **7**, R100 (2006).
30. Fuchs, F. *et al.* Clustering phenotype populations by genome-wide RNAi and multiparametric imaging. *Mol. Syst. Biol.* **6**, 370 (2010).
31. Held, M. *et al.* CellCognition: time-resolved phenotype annotation in high-throughput live cell imaging. *Nat. Methods* **7**, 747–754 (2010).
32. Pau, G., Fuchs, F., Sklyar, O., Boutros, M. & Huber, W. EBImage—an R package for image processing with applications to cellular phenotypes. *Bioinformatics* **26**, 979–981 (2010).
33. Jones, T.R., Carpenter, A.E. & Golland, P. Voronoi-based segmentation of cells on image manifolds. *Comput. Vis. Biomed. Image Appl.* 535–543 (2005).
34. Huber, W., von Heydebreck, A., Sültmann, H., Poustka, A. & Vingron, M. Variance stabilization applied to microarray data calibration and to the quantification of differential expression. *Bioinformatics* **18** (suppl. 1), S96–S104 (2002).
35. Axelsson, E. *et al.* Extracting quantitative genetic interaction phenotypes from matrix combinatorial RNAi. *BMC Bioinformatics* **12**, 342 (2011).
36. Benjamini, Y. & Hochberg, Y. Controlling the false discovery rate: a practical and powerful approach to multiple testing. *J. R. Stat. Soc., B* **57**, 289–300 (1995).